Buckling and failure assessment of curved butt-joint stiffened thermoplastic composite panels with roller boundary conditions

van Dooren, Kevin; Waleson, Jan; Chapman, Mark; Bisagni, Chiara

Important note
To cite this publication, please use the final published version (if applicable).
Please check the document version above.

Buckling and failure assessment of curved butt-joint stiffened thermoplastic composite panels with roller boundary conditions

Kevin van Dooren [a], Jan Waleson [b], Mark Chapman [c], Chiara Bisagni [a,*]

[a] *Delft University of Technology, Faculty of Aerospace Engineering, Delft, The Netherlands*
[b] *GKN Fokker Aerospace, Papendrecht, The Netherlands*
[c] *Gulfstream Aerospace Corporation, United States of America*

ARTICLE INFO

ABSTRACT

Two curved thermoplastic composite multi-stringer panels with roller boundary conditions are analysed and tested to investigate the buckling and failure behaviour. The panels are made of AS4D/PEKK-FC thermoplastic composite, have five stringers with an angled cap on the side and are joined to the skin with the short-fibre reinforced butt-joint technique. The panels have a roller attached to each loading edge, approximating simply-supported boundary conditions to apply compression and bending. One panel has an initial damage representing a barely visible impact damage in one of the stringer butt-joints, and one panel is in pristine condition. Finite element analyses are performed to predict the structural behaviour, and different approximations of the roller boundary conditions are compared. The analyses include material damage initiation and evolution. The out-of-plane displacement of the panels is measured by digital image correlation, and failure is captured with high-speed cameras. The panels fail in a sudden manner when the cap separates from the web, followed by web failure and skin–stringer separation in the butt-joint. The numerical analysis predicts the overall structural behaviour but cannot capture well the sudden panel collapse due to material damage.

1. Introduction

One of the prominent goals of the aeronautical industry is to lower the environmental impact of flight by reducing fuel consumption, which also reduces costs. One of the ways is to reduce the structural weight, as the weight is directly related to the fuel consumption for flight. The reduction of weight can also lead to a higher passenger capacity per flight, leading to a lower number of flights needed.

This research targets the reduction of the aeronautical structural weight by the use of thermoplastic composites and by allowing these structures to buckle below the ultimate load. Aeronautical structures mostly consist of stiffened, thin-walled designs, which are known to buckle for compression and shear load cases. The current designs of primary structures do not allow for buckling below the ultimate load, as the post-buckling behaviour and failure modes in the post-buckling field are yet to be fully understood. It has been shown that these structures can sustain load deep into the post-buckling field [1,2], indicating a considerable weight-saving potential.

The use of thermoplastic composites can also lead to a reduction of structural weight due to their structural properties and new manufacturing techniques. They are known to be more ductile and to have a higher toughness compared to their thermoset counterpart [3,4]. Thermoplastics allow for manufacturing techniques such as welding [5,6] and co-consolidation [7], which lower the amount of fasteners needed and decrease both the weight and production time [8].

The common failure modes in post-buckling of aerospace stiffened structures consist of material failure [9–11] and skin–stringer separation [12–15], which are researched mostly on thermoset composites. The investigations on these failure modes are executed on a wide variety of specimen designs, consisting of single [16] and multi-stringer [17] panels with closed omega stiffeners [18], blade stiffeners [19,20] and I shaped stiffeners [21]. The tested specimens can be in both pristine and damaged state. The damage can consist of, for example, impact damage [22], or an approximation of Barely Visible Impact Damage (BVID) by including a foil at the skin–stringer interface to create a pre-existing separation without inflicting actual impact damage [23].

The post-buckling behaviour of co-consolidated multi-stringer panels utilizing the butt-joint technique [1,7] is investigated in this research by analysis and experiments. Two multi-stringer panels are designed and manufactured by GKN Fokker [24]. The panels have a convex curvature and five stringers on the outside of the curvature. One

panel has initial damage at the skin–stringer interface that represents BVID and one panel is in pristine condition. The panels are loaded in a mixed bending and compression load case, thanks to the aluminium rollers attached on both loading edges, to which compression is applied in a testing machine. These boundary conditions are uncommon in aeronautics, with literature limited to sandwich structures [25,26]. Compression tests of aerospace structures typically involve clamped boundary conditions for the loading edges, achieved by potting the edges with epoxy or similar methods [27,28]. Roller boundary conditions are, however, more common in naval and civil applications, for example, for research on stiffened steel plates with single-stringer [29] and multi-stringer specimens [30,31], but also aluminium plates with both open and closed-section stiffeners [32,33] and even testing of corrugated board panels of packaging material [34]. The reason for using the roller boundary conditions in this research is twofold. Firstly, testing a panel with curvature in the longitudinal direction in compression with clamped-like conditions achieved by square loading blocks can lead to tilting and rotation of these blocks due to the resulting moments, and it would not allow achieving structural behaviour in post-buckling representative of an aeronautical structure. Secondly, the rollers allow rotation and consequentially allow to achieve deformations, which would usually require a longer panel with clamped-like boundary conditions. This research investigates the post-buckling and failure behaviour of convex butt-joint panels with roller boundary conditions, to increase the understanding of post-buckled thermoplastic composite structures and of the critical failure modes for this new joining technique.

2. Butt-joint stiffened thermoplastic composite panels

The curved multi-stringer panels represent the fuselage section of a business jet, where double curvature can be present in the tail section with a convex shape. The panels are manufactured and potted to the rollers by GKN Fokker and are received as shown in Fig. 1. The rollers are made of aluminium, and the panels are attached to the rollers with epoxy potting. The panels have an approximate radius of curvature and length of 6277 and 497 mm, respectively, and the total length including rollers is 585 mm, as reported in Fig. 2(a). The rollers have a radius of 45 mm, and the loading edge and bending neutral axis of the panels coincide with the rollers' centre of curvature. The panels have five stringers, with a stringer spacing of 152.4 mm, which results in a total width of 650 mm, as reported in Fig. 2(c).

The butt-joint technique is used to join the stringer to the skin. The stringer consists of a web and an angled side cap. The cap is 15 mm wide, angled at an angle of 105 degrees w.r.t. the web, which is 28 mm in height, as reported in Fig. 2(b). The skin–web joint, which is called the butt-joint, and the web-cap joint consist of carbon Short Fibre Reinforced Plastic (SFRP) filler PolyEtherKetoneKetone (PEKK) extrusion profiles, of which the material properties are reported in Table 1. One of the panels has initial damage at the skin–stringer interface that represents a BVID. The location of this BVID is highlighted in red in Fig. 2(a, b). The BVID is created by including a 40 mm foil at the skin–stringer interface during co-consolidation, after which the BVID is extended to 70 mm by applying out-of-plane displacement to the skin in a test machine [1,35]. In this procedure, the skin is supported from the bottom of the skin at two locations. Then out-of-plane displacement is applied to the skin away from the stringer, in between the supports at the location of the foil in the middle of the panel.

The laminated parts are made of Fast Crystallizing PolyEtherKetoneKetone (PEKK-FC) carbon fibre (ASD4) UniDirectional (UD), of which the properties are reported in Table 2(a), and of additional glass fabric patches, of which the assumed properties are reported in Table 2(b). The layups of the laminates are reported in Table 3. The three different skin layups are due to the glass fabric patches applied underneath the stringer. The skin is manufactured by advanced fibre placement, while the web and cap laminates are pre-forms cut from a

Table 1
Properties of PEKK carbon SFRP filler [1].

E_{11} [MPa]	$E_{22} = E_{33}$ [MPa]	v_{12} [–]	G_{12} [MPa]	ρ [kg/m^3]
13 252	6579	0.42	2389	1560

Table 2
Ply properties of: (a) AS4D/PEKK-FC carbon UD ply [1]; (b) PEKK glass fabric [1].

	E_{11} [MPa]	E_{22} [MPa]	v_{12} [–]	G_{12} [MPa]	ρ [kg/m^3]	t_{ply} [mm]
a	126 100	11 200	0.3	5460	1560	0.138
b	25 000	25 000	0.3	3000	2200	0.1

Table 3
Layups and nominal thicknesses of laminate sections, with C and G superscript for carbon and glass plies, respectively.

Section	Thickness [mm]	Layup
Skin L1	2.484	$[45/-45/0/45/90/-45/45/0/-45]^C s$
Skin L2	2.684	$[0_2]^G[45/-45/0/45/90/-45/45/0/-45]^C s$
Skin L3	2.884	$[0_4]^G[45/-45/0/45/90/-45/45/0/-45]^C s$
Web	2.484	$[45/90/-45/0/45/0/-45/0/\underline{45/-45}]^C s$
Cap	2.760	$[45/90/-45/0/45/0/-45/0/0/90]^C s$

larger laminate. The web and cap are then assembled with the short fibre filler extrusion profiles and tooling blocks in an inner mould. The skin is placed on top of the mould, followed by the placement of the glass fibre patches at the stringer locations. The assembly is then vacuum-bagged and co-consolidated in an autoclave.

The panels are instrumented with 18 strain gauges at the positions reported in Fig. 2(d), in the middle of the panel along the longitudinal direction. Strain gauges are attached back-to-back on the skin on the free edges, in the middle of the outer bays, underneath each stringer and on the top of the vertical web. They can capture loading imperfections and allow to determine how the load is redistributed due to buckling, material damage and skin–stringer separation.

White paint and black speckles are then applied on both sides of the panels as well as on the flat surfaces of the rollers.

3. Numerical methodology

The post-buckling behaviour of the curved multi-stringer panels is analysed with the commercial Finite Element (FE) software Abaqus 2021 [36].

The model utilizes continuum shell elements (SC8R) for the composite laminates, while solid brick and wedge elements (C3D8I, C3D6) are used for the short fibre filler material. The epoxy potting and aluminium rollers consist of solid brick elements with reduced integration (C3D8R) for better computational efficiency. The mesh of the stringer and skin cross-section is reported in Fig. 3.

Dynamic implicit analysis is used in this study. The implicit step adopts a quasi-static application with a backward Euler operator. The total step time is 1 s, with the initial and maximum time increment size set to 0.01 s and the minimum to 1e-8 s. To improve convergence when separation starts, the maximum number of attempts for an increment is increased to 40 in the time incrementation controls.

3.1. Comparison of boundary condition approximation

The roller boundary condition is approximated in three ways, as shown in Fig. 4.

The first method utilizes a reference point in the centre of the roller radius, as shown in Fig. 4(a). This reference point is tied to the region of the panel that is inside the potting material, but no actual potting material is modelled. The reference point is constrained in all degrees

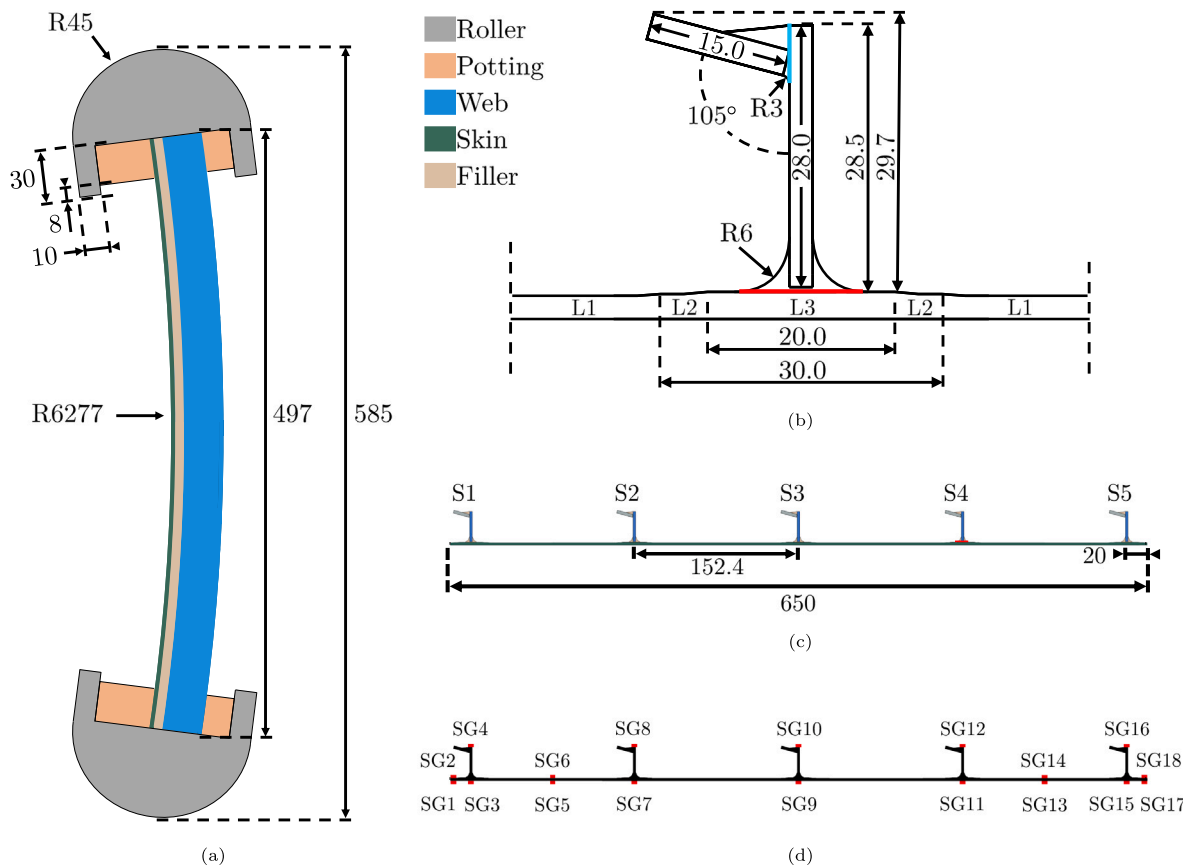**Fig. 1.** Panel: (a) stringer-side; (b) skin-side.

Fig. 2. Panel geometry: (a) side-view illustration ; (b) stringer cross-section; (c) panel cross-section; (d) strain gauge positions.

of freedom except for rotation of the axis in the centre of the roller radius, and compression is applied in the longitudinal direction.

The second method models the potting and roller as shown in Fig. 4(b). The panel, potting and roller are connected with shared nodes. There is a reference point in the centre of the roller radius, which is tied to a small region on the outside of the roller radius. This region is kept small to approximate a contact area. The reference point is free to rotate around the axis in the centre of the roller radius, compression is applied in the longitudinal direction, and the remaining degrees of freedom are constrained. The load is transferred from the reference point to the contact area through the rigid body ties. This method aims to approximate the application of compression through contact

without the need for a contact definition and improves computational efficiency.

The third method adds contact between the roller and a contact surface to apply compression, as shown in Fig. 4(c). This method still uses a reference point in the centre of the roller radius, which is tied to a region on the outside of the roller. This region is to the left of the initial contact point of the roller with the contact surface. It does not come into contact with the contact surface, as the roller rotates in an anti-clockwise direction under compression. The reference point is constrained in all degrees of freedom except for rotation around the axis in the centre of the roller radius and the longitudinal direction. The purpose of the reference point is to keep the panel in place and
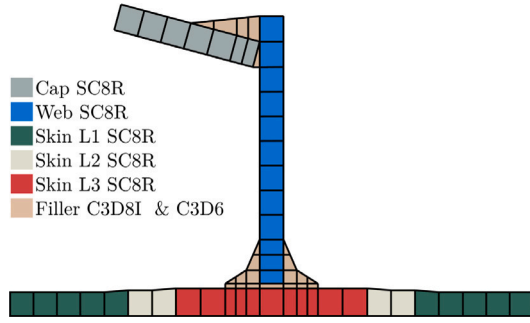
Fig. 3. Mesh of the stringer cross-section.

Table 4
Strength and fracture properties of AS4D/PEKK-FC carbon UD ply [1,5].

X^T [MPa]	X^C [MPa]	Y^T [MPa]	Y^C [MPa]	S^L [MPa]
2559	1575	83.1	284	99

G_{X^T} [kJ/m^2]	G_{X^C} [kJ/m^2]	G_{Icp} [kJ/m^2]	G_{IIcp} [kJ/m^2]	
125	61	1.12	2.35	

shed the need for modelling friction, as it is assumed that there is no slipping of the rollers in the test.

The three models are compared using a mesh size of 2.5 mm for the laminated parts. The models with potting have a variable mesh size for the potting, ranging from 2.5 mm to 10 mm. The mesh size of 2.5 mm is where the potting is connected to the panel with shared nodes, and it increases in size in an outwards direction and is 10 mm in size at the connection with the roller. The roller uses a similar meshing technique, with the mesh size also ranging from 2.5 mm to 10 mm, for the model without contact. The model with contact uses a locally refined mesh at the contact surface of 1 mm.

All analyses use the same total displacement of 6 mm. The analysis of the three models run on the same CPU, and the wall clock time is 1589 s, 3837 s and 4752 s, respectively. It should be noted, however, that the model with contact has an initial clearance between the contact surface and roller and displaces the roller 5.78 mm in total, which could lead to a slightly lower wall clock time.

The load–displacement graph of the three analyses is reported in Fig. 5(a). The difference in load–displacement behaviour is minimal between the three different boundary condition methods. Method 1 shows an initial higher stiffness compared to methods 2 and 3 but converges with method 3 at higher displacements. Method 2 matches with method 3 initially but shows a slightly lower load at higher displacements. The roller load-rotation of the three analyses is reported in Fig. 5(b). Only the top roller rotation is reported for conciseness, as the rotation of both rollers is indistinguishable in the analysis. All analyses show similar behaviour, with method 3 initially presenting a higher rotational stiffness and method 2 having a lower overall stiffness. The two outer stringers, stringers 1 and 5, displace in the lateral direction during loading, as illustrated in Fig. 6(a). The maximum lateral displacement of stringer 1 and minimum of stringer 5 are reported in Fig. 6(b) and (c), respectively. Method 2 and 3 have very similar behaviour, while method 1 has a higher stiffness, especially for stringer 1. This is most likely caused by the rigid body tie in the potting region of method 1, instead of the physical modelling of the potting for methods 2 and 3.

This comparison shows that method 1 is an efficient option for a similar load–displacement behaviour compared to method 3, which should be the method closest to reality. However, taking into account the differences in the deformation of the panel and the implementation of damage evolution in the following analyses, method 2 is considered a good compromise in terms of results and computational time. All analysis results in the following sections are obtained using method 2.

3.2. Damage and mesh size sensitivity

The Hashin criterion [37] is included in the analysis for initiation of material damage, followed by damage evolution [38]. The criteria for fibre tension, fibre compression, matrix tension, and matrix compression failure are reported in Eqs. (1)–(4). The criteria are expressed as

F, with superscript t and c for tension and compression, respectively, and subscript f and m for fibre and matrix, respectively. A value of 1 or higher means the criterion is met. The equations consist of the components $\hat{\sigma}_{11}$, $\hat{\sigma}_{22}$ and $\hat{\tau}_{12}$, for fibre direction, matrix direction and shear, from the effective stress tensor. The remaining terms are the material strengths, with X^T and X^C for fibre tension and compression strength, Y^T and Y^C for matrix tension and compression strength, and lastly, S^L for shear strength. The material strength properties for the criteria and the fracture properties are reported in Table 4. The fracture properties consist of the energies dissipated during damage evolution, with G_{X^T} for fibre tension, G_{X^C} for fibre compression, G_{Icp} for matrix tension and G_{IIcp} for matrix compression damage.

Fibre tension $(\hat{\sigma}_{11} \geq 0)$

$$F_f^t = \left(\frac{\hat{\sigma}_{11}}{X^T} \right)^2 \tag{1}$$

Fibre compression $(\hat{\sigma}_{11} < 0)$

$$F_f^c = \left(\frac{\hat{\sigma}_{11}}{X^C} \right)^2 \tag{2}$$

Matrix tension $(\hat{\sigma}_{22} \geq 0)$

$$F_m^t = \left(\frac{\hat{\sigma}_{22}}{Y^T} \right)^2 + \left(\frac{\hat{\tau}_{12}}{S^L} \right)^2 \tag{3}$$

Matrix compression $(\hat{\sigma}_{22} < 0)$

$$F_m^c = \left(\frac{\hat{\sigma}_{22}}{Y^C} \right)^2 + \left(\frac{\hat{\tau}_{12}}{S^L} \right)^2 \tag{4}$$

A mesh size sensitivity study is executed incorporating material damage and damage evolution, which are also compared to the results without damage evolution. The considered mesh sizes are 0.75, 1.25 and 2.5 mm, with one element through the thickness of the composite laminates. The load–displacement results are reported in Fig. 7. The analyses with damage evolution start to show material softening at 2.56 mm of displacement for a mesh size of 2.50 mm, and at 2.50 mm of displacement for a mesh size of 1.25 and 0.75 mm, which can also be partially attributed to increment timing. At higher displacements, however, there is a sensitivity to mesh size, with a larger mesh size leading to more softening. The difference is more pronounced between the analysis with a mesh size of 1.25 and 2.5 mm, above an applied displacement of 4 mm. Consequently, the analysis results in the following sections are obtained using a mesh size of 1.25 mm.

3.3. Skin–stringer separation

It is chosen to model skin–stringer separation only in the panel with BVID, and not in the pristine panel. The skin–stringer interface of the stringer with BVID is investigated using a contact pair definition with the Virtual Crack Closure Technique (VCCT) for a partial bond. The bonded area is approximately 445 mm long and 9.7 mm wide, with 70 mm not bonded in the middle of this area to account for the BVID. In the model, separation can only occur in between the filler and skin, and no crack migration into the filler is allowed to lower the complexity of the model. This assumption is based on the failure
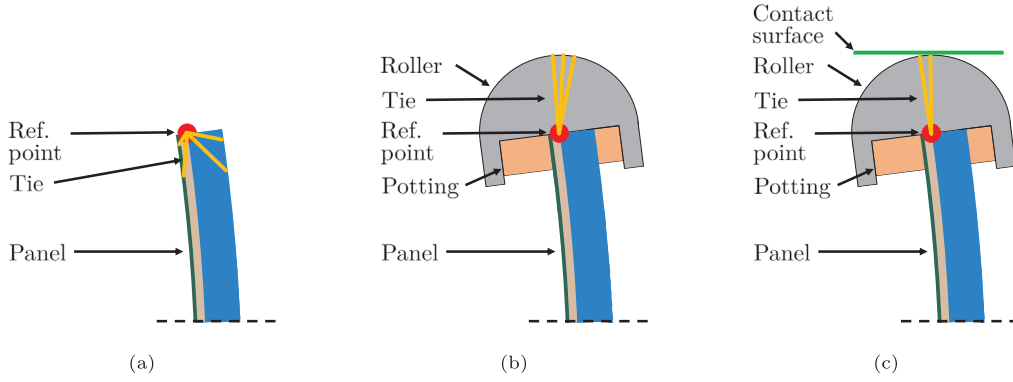
Fig. 4. Comparison of the three approximations of the roller boundary conditions: (a) method 1, panel only; (b) method 2, roller; (c) method 3, roller with contact.
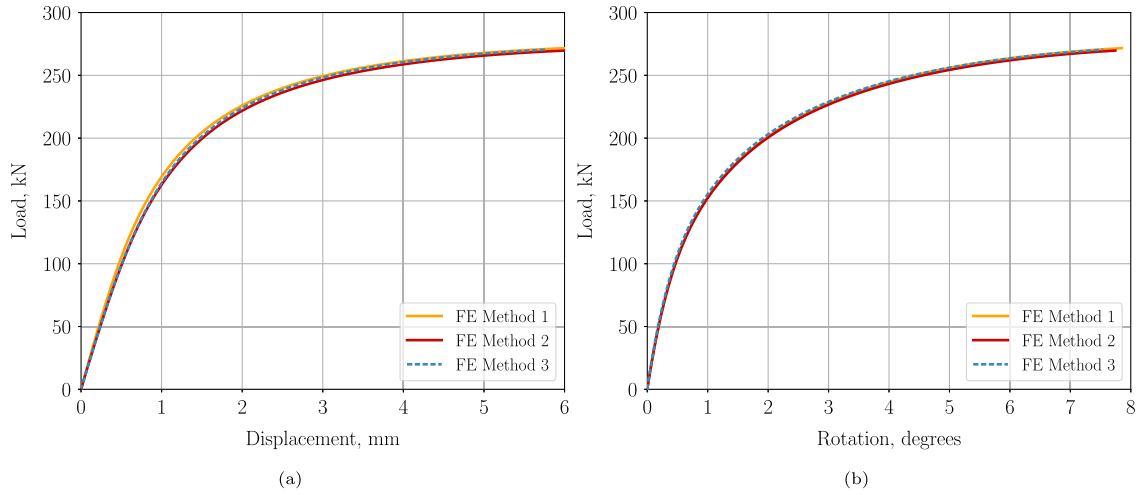

Fig. 5. Load displacement (a) and rotation (b) curves of the analyses with different boundary conditions.

behaviour of compression tests of three-stringer panels [1] and three-point bending tests on single-stringer specimens [39]. VCCT is chosen over the cohesive zone method based on results achieved in previous work [1], where VCCT is chosen because of the coarser mesh-size requirement [40,41].

The VCCT definition includes mixed-mode interface behaviour with the Benzeggagh Kenane (BK) criterion [36,42], for which the equations are reported in Eqs. (5) and (6). The equations for the critical equivalent strain energy release rate G_{equivC} and the equivalent strain energy release rate G_{equiv} consist of the fracture toughness of the three different modes: G_{IC}, G_{IIC} and G_{IIIC}, and the strain energy release rates of each mode: G_I, G_{II} and G_{III}. Fracture of the interface occurs when G_{equiv} divided by G_{equivC} is equal or greater than one. The strain energy release rates are based on the nodal forces and displacements. The fracture toughness of mode 1 and 2 are based on internal tests of GKN Fokker, and it is assumed that the fracture toughness of mode 3 is equal to mode 2. The BK parameter, η, of a similar thermoplastic composite is used, of which the properties are available in literature [43]. The interface properties are reported in Table 5.

$$G_{equivC} = G_{IC} + (G_{IIC} - G_{IC}) \left(\frac{G_{II} + G_{III}}{G_I + G_{II} + G_{III}} \right)^{\eta} \tag{5}$$

$$G_{equiv} = G_I + G_{II} + G_{III} \tag{6}$$

The fracture tolerance and unstable crack growth tolerance of the VCCT definition are 0.2 and 10, respectively. Allowing multiple nodes to be released within one increment with the unstable crack growth option can improve convergence and computational efficiency. The contact pair definition uses node-to-surface contact discretization, with

Table 5
Fracture properties of skin–stringer interface [1,43].

G_{IC} [kJ/m^2]	G_{IIC} [kJ/m^2]	G_{IIIC} [kJ/m^2]	η [–]
1.41	1.9	1.9	2.3

the filler material as the master and the skin as the slave surface. Contact stabilization is enabled with a stabilization factor of 1e−4.

4. Test setup

The curved multi-stringer panels are tested to investigate the post-buckling behaviour and the final failure mode and to validate the numerical analysis. A MTS test machine is used, which is capable of 3500 kN in compression.

The experimental test setup is shown in Fig. 8 from the stringer-side of the panel (a), from the skin side (b) and with a top-view illustration (c). A female test fixture is clamped to the top compression plate and base of the test machine. The female test fixture is a machined aluminium profile with vertical uprights to limit the movement of the rollers, and to which white paint and black speckles are applied for Digital Image Correlation (DIC). The top and bottom female text fixtures are aligned such that the uprights on the right side, as seen in Fig. 8(b), can be used to align the panel at the start of the test. The top fixture has hangers mounted to the side to catch the top roller in case of panel collapse. The inner width of the fixtures is 102 mm, which is 12 mm wider than the rollers. This allows for free rotation of the rollers
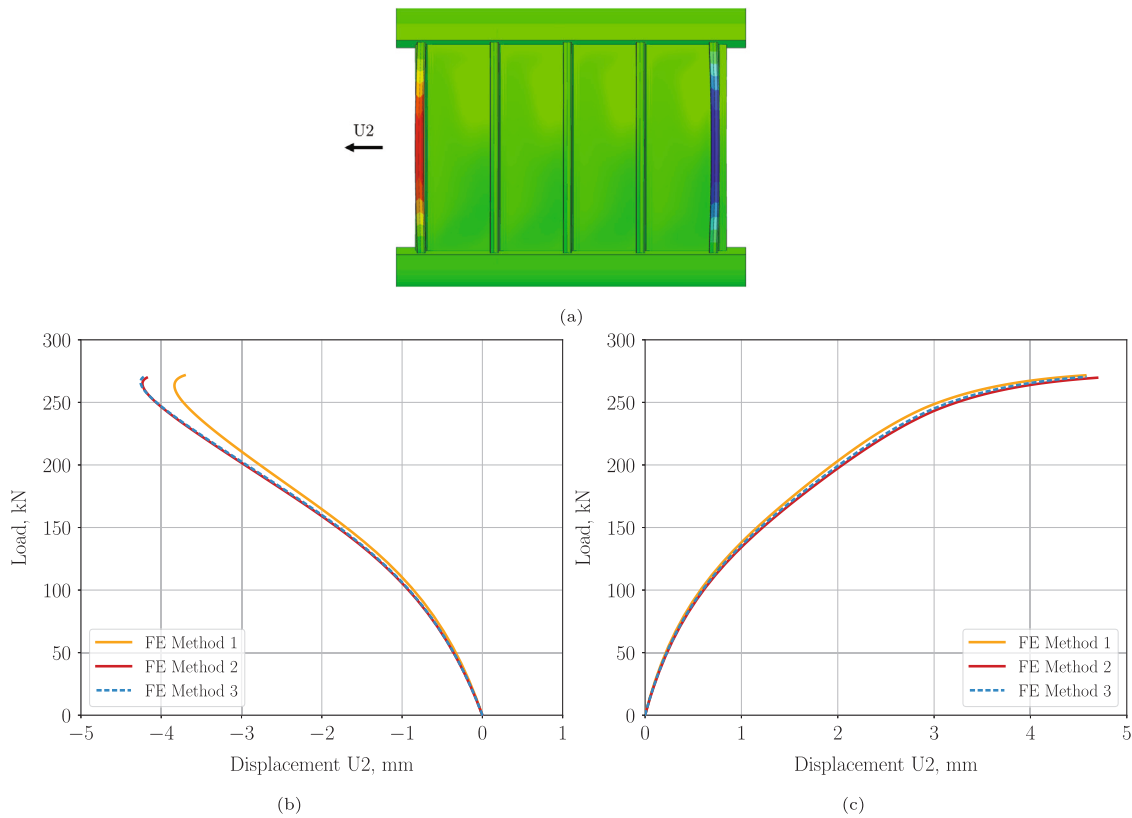
(a)

(b)

(c)

Fig. 6. Load versus lateral displacement of the analyses with different boundary conditions: (a) contour plot FE method 2; (b) negative displacement; (c) positive displacement.
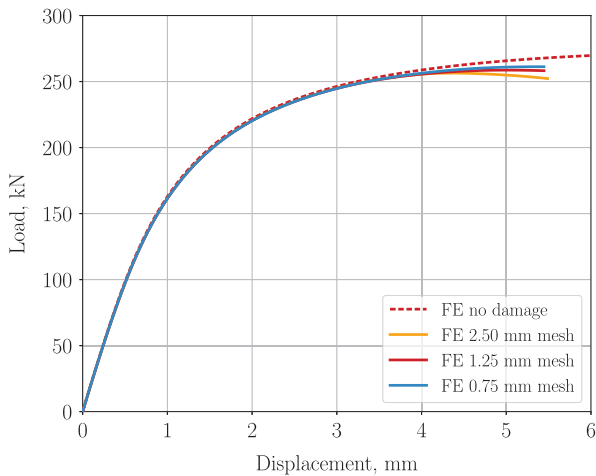

Fig. 7. Load displacement curves of mesh-size sensitivity study of damage.

without touching the vertical uprights. When compression is applied, the panel rolls to the left. When the panel fails, the female test fixtures are able to keep the panel in place. After panel alignment, a preload of approximately 2 kN is applied to keep the panel in place.

The tests of panel 1 and panel 2 are executed at a loading rate of 0.25 mm/min. The force is measured by the load-cell of the MTS test machine and the displacement of the compression plate is measured by three Linear Displacement Sensors (LDS). Two LDS are placed next to the panel and one LDS is placed on the corner of the compression plate. The different locations allow to determine load imperfections, as shown in Fig. 8(c).

The displacement field of the panels is measured by two DIC systems, one system on the stringer side of the panel and one system on the skin side of the panel. The systems have two cameras each, and the pictures are post-processed with VIC 3D 8. This measurement allows to determine the buckling shape from the out-of-plane displacement of the skin, the longitudinal shortening from the in-plane displacement of the female text fixtures, and the rotation of the rollers from the out-of-plane displacement.

The tests are also captured with four GoPro cameras, one placed on the skin-side, one placed on the stringer-side, and one placed on each lateral side of the panel. The cameras record phenomena such as buckling and skin–stringer separation events, besides capturing the sound of events which might not be visible, such as material failure.

Two high-speed cameras are used to record the final failure of the panels. One camera is placed on the cap-side of the stringers, focusing on the middle three stringers, that captures at 5600 and 5200 fps for the test of panels 1 and 2, respectively. The second high-speed camera is placed next to DIC system 2, which captures the whole panel at 10 000 fps for panel 1 and 9600 fps for panel 2.

5. Test and numerical results

This section discusses the results of the tests till failure of the two panels and compares them to the numerical analysis. Panel 1 was pre-tested till a displacement of 4.56 mm, which did not lead to failure, and the panel was then tested till failure. This section will only include the results of the test till failure for conciseness.

5.1. Load versus displacement curves

The load–displacement curves of the tests and numerical analysis are reported in Fig. 9. The panels show a decreasing stiffness due to the curved geometry and roller boundary condition, clearly seen at loads above approximately 120 kN. At higher loads close to failure, the load–displacement behaviour starts to plateau. The stiffness of panel 1 and panel 2 are similar. The stiffness of panel 1 is slightly lower between
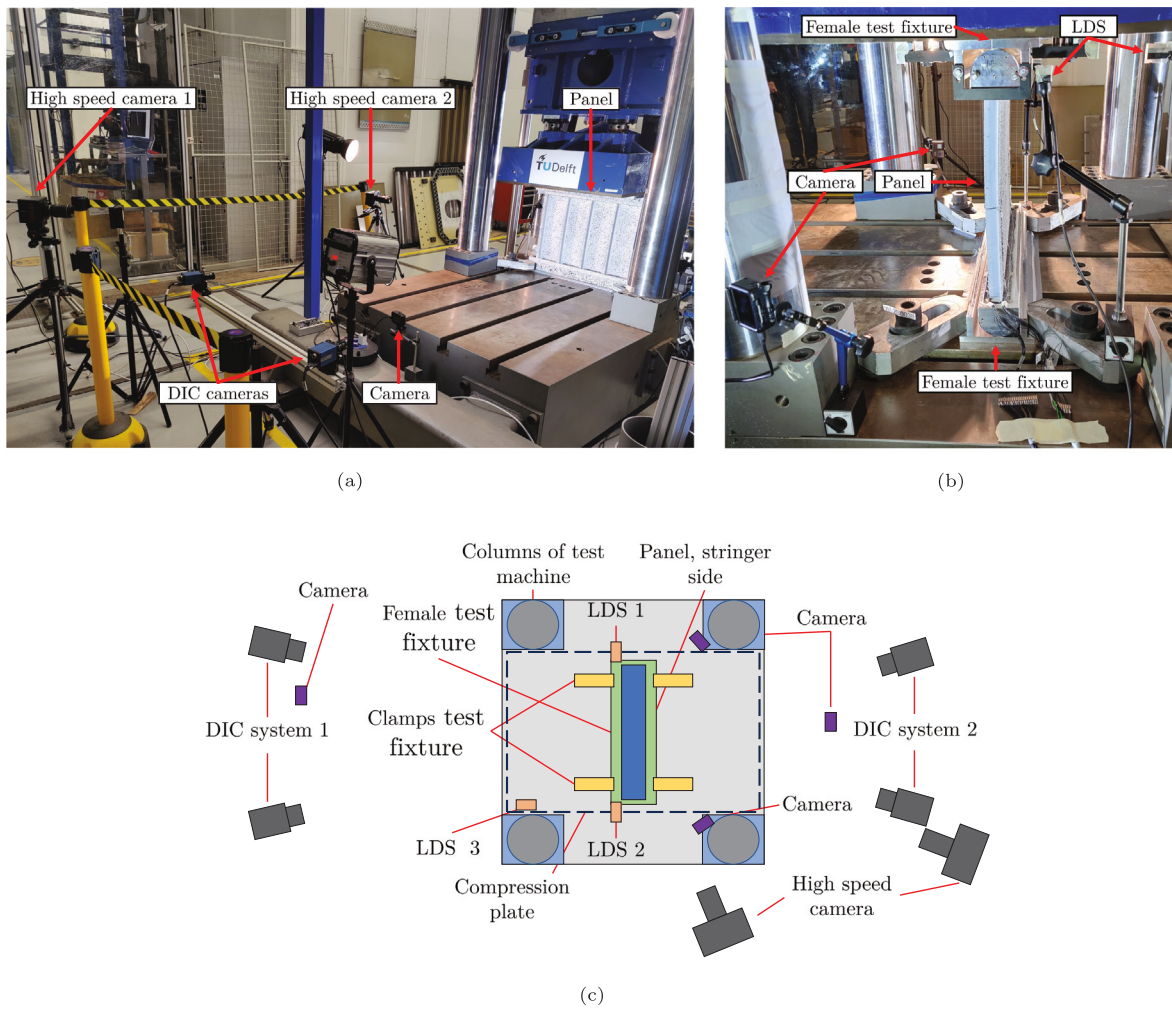
(a)

(b)

(c)

Fig. 8. Test setup: (a) stringer side; (b) side-view; (c) top-view illustration.

approximately 1 and 4 mm of displacement, which can be caused by material softening due to the pretest. Panel 1, with BVID, fails at a load of 251 kN and 5.22 mm of displacement, while panel 2 fails at a load of 249 kN and 5.06 mm of displacement. Unexpectedly, the panel with BVID shows a slightly higher failure load and displacement, which indicates that the BVID is not critical for the failure mode that causes the collapse.

The numerical analysis predicts the initial stiffness well, but above 100 kN it starts to over-predict the stiffness. However, the plateau behaviour at higher loads is predicted well. The analysis with VCCT is conservative in predicting failure due to skin–stringer separation, which did not appear to be the critical failure mode in the test. The following sections, therefore, only show results from the analysis without VCCT.

5.2. Load versus rotation curves

The rotation is calculated from the average out-of-plane location of the top and bottom half of the flat vertical plane of the rollers, as measured by DIC, in combination with the height of this plane. The load-rotation curves of the tests and numerical analysis are reported in Fig. 10. The load-rotation curves are similar to the load–displacement curves, with a decreasing stiffness with an increase in load and a plateau at higher applied displacements. There is a small difference in rotation between the top and bottom rollers initially for all tests, which stays constant after settling. Panel 1 seems to have a slightly lower amount of rotation than panel 2, indicating a higher bending stiffness.
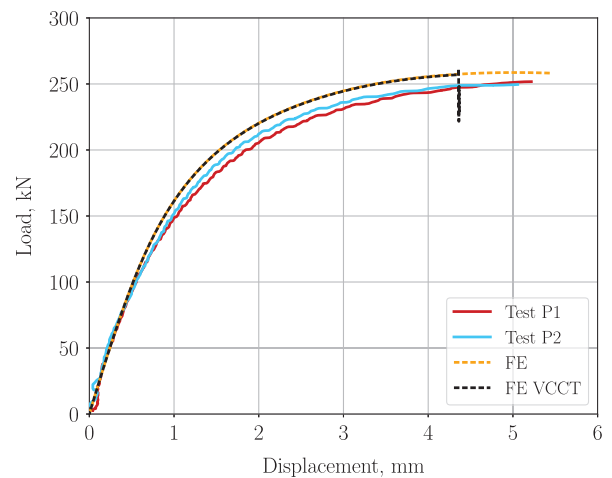

Fig. 9. Load–displacement curves from tests and numerical analysis.

The numerical analysis predicts the rotation of the rollers well, with an under-prediction of the rotation at higher loads, above approximately 1.5 and 3 degrees of rotation for panels 1 and 2, respectively.
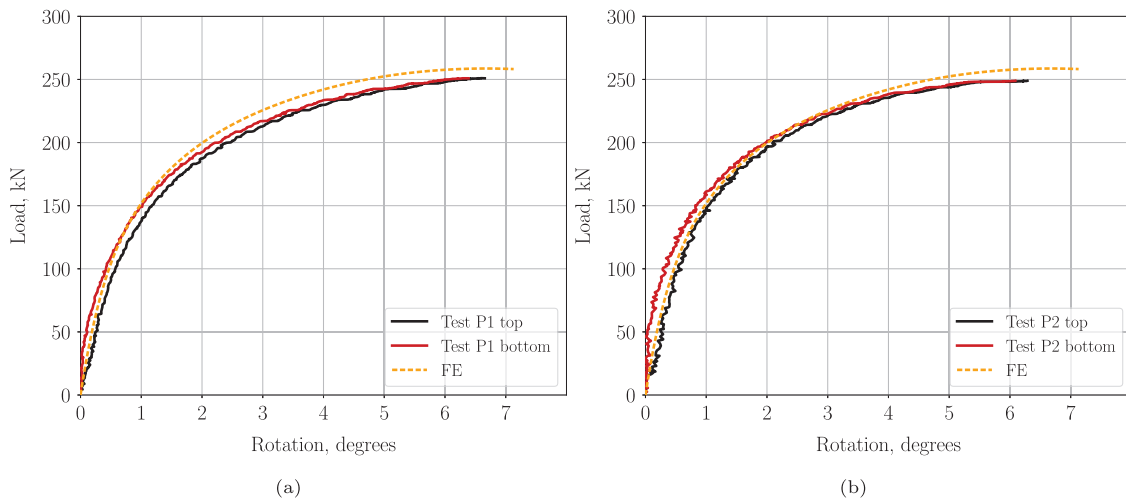
Fig. 10. Load-rotation curves from tests and numerical analysis: (a) panel 1; (b) panel 2.

5.3. Strain gauge curves

The measured strains of the test till failure of panel 2 are reported in Fig. 11. The strains of panel 1 are not reported for conciseness, as there is a high level of similarity with panel 2. The strains measured by the skin strain gauges show negative strains, indicating compression, and the strain gauges on top of the stringer webs show positive strains, indicating tension. This is due to the combined compression and bending loading. The strains also reach higher values than the more typical compression tests, with strains up to 19 400 microstrain. The strains show a slight loading imperfection in the skin, while the stringers are equally loaded. The outer stringers, strain gauges 4 and 16, do show differences, but this can also be caused by geometric differences instead of a loading imperfection. The highest strains are in the stringer area and free edges, with lower strains in the middle of the bay.

The numerical analysis predicts the overall behaviour well, with a similar over-prediction of stiffness, and thus under-prediction of strain, at higher loads as for the load–displacement curves. The analysis does not consider loading imperfections, which is most noticeable for strain gauges 17 and 18. The strains in the stringer region seem slightly better predicted than in the skin region.

5.4. Out-of-plane displacement

The out-of-plane displacement of the skin is measured during the tests by DIC, and is reported in Fig. 12. The scale of the contour plot is based on the out-of-plane displacement of the skin at the maximum load. For each plot, an offset is applied to the displacement field, such that the scale's maximum is at the maximum out-of-plane displacement point of the panel. This eliminates the contribution of the rolling motion of the panels to the out-of-plane displacement and results in a clearer comparison.

The out-of-plane displacement of the test of panel 1 is plotted in Fig. 12(a–e) in steps of 1 mm of longitudinal applied displacement and at the maximum applied displacement. The panel shows a single half-wave in each bay, with the highest out-of-plane displacement at the left side of the panel. The evolution of the out-of-plane displacement is gradual, with an exponential increase of displacement w.r.t. the load. The three bays on the right initially have similar out-of-plane displacement, but at higher applied displacement, the bay on the rightmost side starts to have higher displacement than the middle two bays. At the maximum applied displacement, the difference in out-of-plane displacement is 2–2.5 mm between the middle two bays and most left bay, and a 1 mm difference between the most left and right bay. These differences can be due to loading imperfections but are also due

to geometric differences. The middle two bays are stiffer due to the adjacent bays, while the two outside bays have a free edge nearby. The difference between the most left and right bay is partly due to the anti-symmetric stringer, which provides more stiffness when the cap is pointed towards the bay. In terms of loading imperfections, the differences can be due to both the difference in applied compression between left and right, in terms of roller rotation and the resulting out-of-plane displacement of the roller itself. With only a 1 mm difference in out-of-plane displacement between the most left and right bay, and considering the geometric differences, the loading imperfections are estimated to be small.

The out-of-plane displacement of the test of panel 2 till failure is plotted in Fig. 12(f–j). The out-of-plane displacement behaviour of panel 2 is similar to panel 1, in terms of total out-of-plane displacement and the differences between the four bays. There is no visible difference in the out-of-plane displacement of panel 1 and 2 due to the BVID of panel 1.

The out-of-plane displacement of the numerical prediction is reported in Fig. 12(k–o). The numerical analysis accurately predicts the out-of-plane displacement behaviour, with only minimal differences due to loading and geometric imperfections not considered in the analysis. The differences between the bays are lower than what is measured in the tests, with the most left and right bays having a 0.3 mm difference in out-of-plane displacement at 5 mm of applied displacement, and the middle two bays a 1 mm difference compared to the outer bays.

5.5. Panel collapse

High-speed cameras are used to capture the collapse of the panels at a frame rate of 10 000 fps for panel 1 and 9600 fps for panel 2. For the test of panel 1, the camera is positioned such that the BVID in the butt-joint is visible from the cap-side of the stringers, which results in only four visible stringers. This is, however, considered acceptable, as the stringers at the edges are not the main priority. The camera is positioned to the right side during the test of panel 2. The whole panel is captured, which requires lowering the frame rate to 9600 fps to compensate for the higher resolution.

The panel collapse sequence of panel 1 is reported in Fig. 13 over a total time period of 1.1 ms. Panel collapse starts with the cap separating from the web of stringer 4 (a), the stringer with a BVID in the butt-joint skin–stringer interface. The cap completely separates in the following two frames and fractures at the top of the panel (b–c), followed by failure of the web (d). Then, the cap of stringer 3 separates from the web (e), and the cap fractures at the bottom of the panel (f). The web
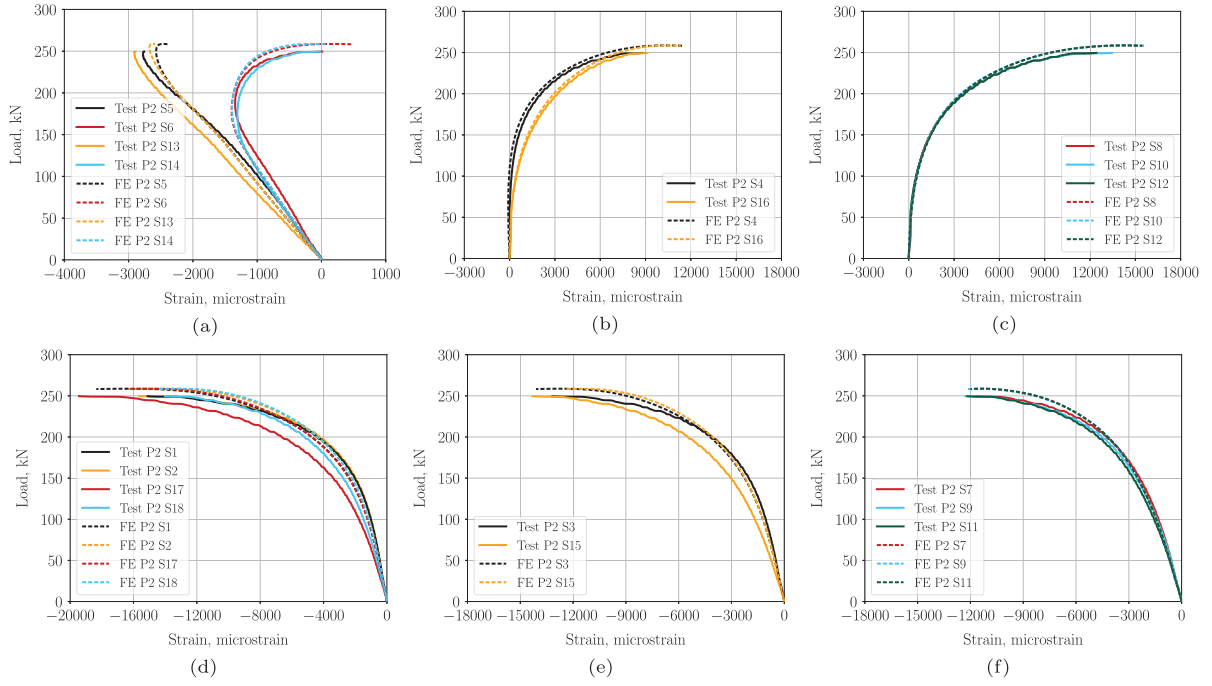
Fig. 11. Experimental and numerical compressive strains of panel 2 in pristine condition: (a) bays; (b) top of side stringers; (c) top of middle three stringers; (d) free edges; (e) bottom of side stringers; (f) bottom of middle three stringers.
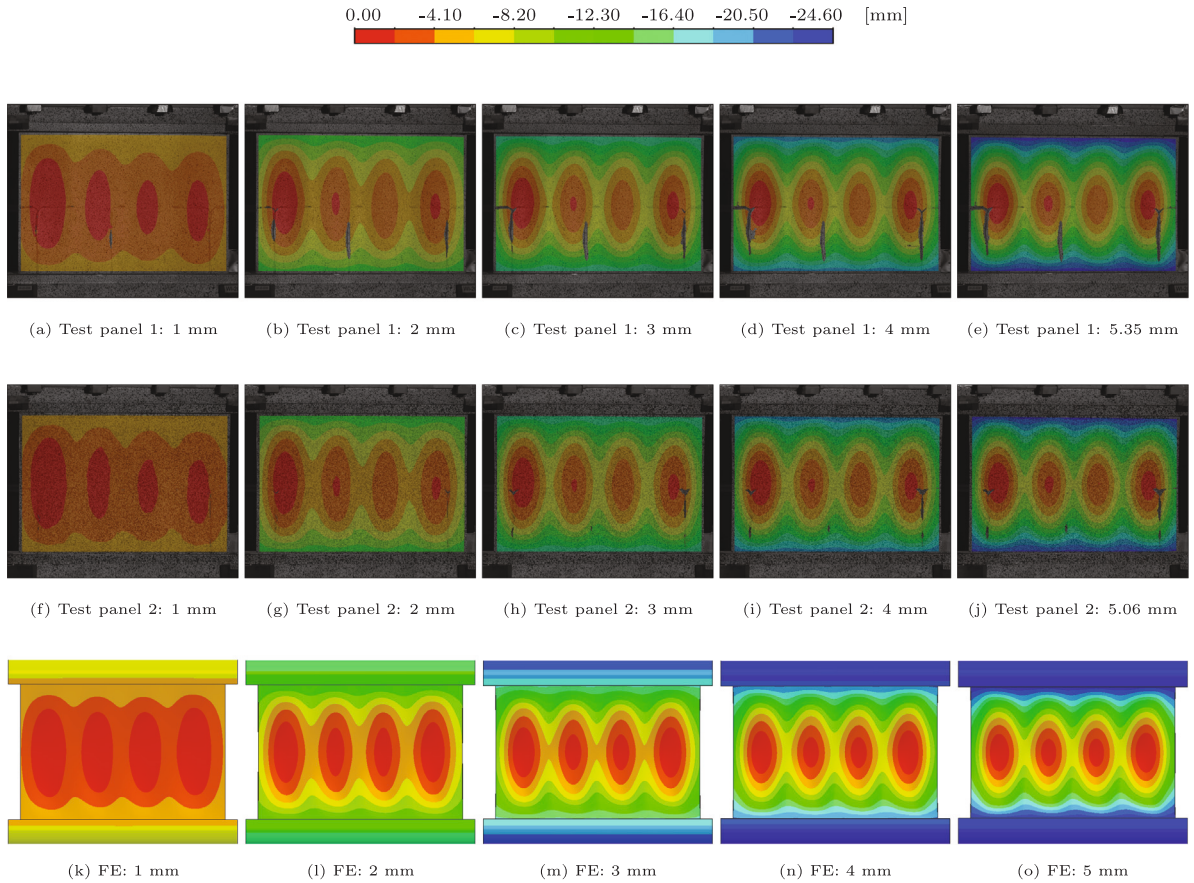
Fig. 12. Out-of-plane displacement: (a–e) test panel 1; (f–j) test panel 2; (k–o) FE.
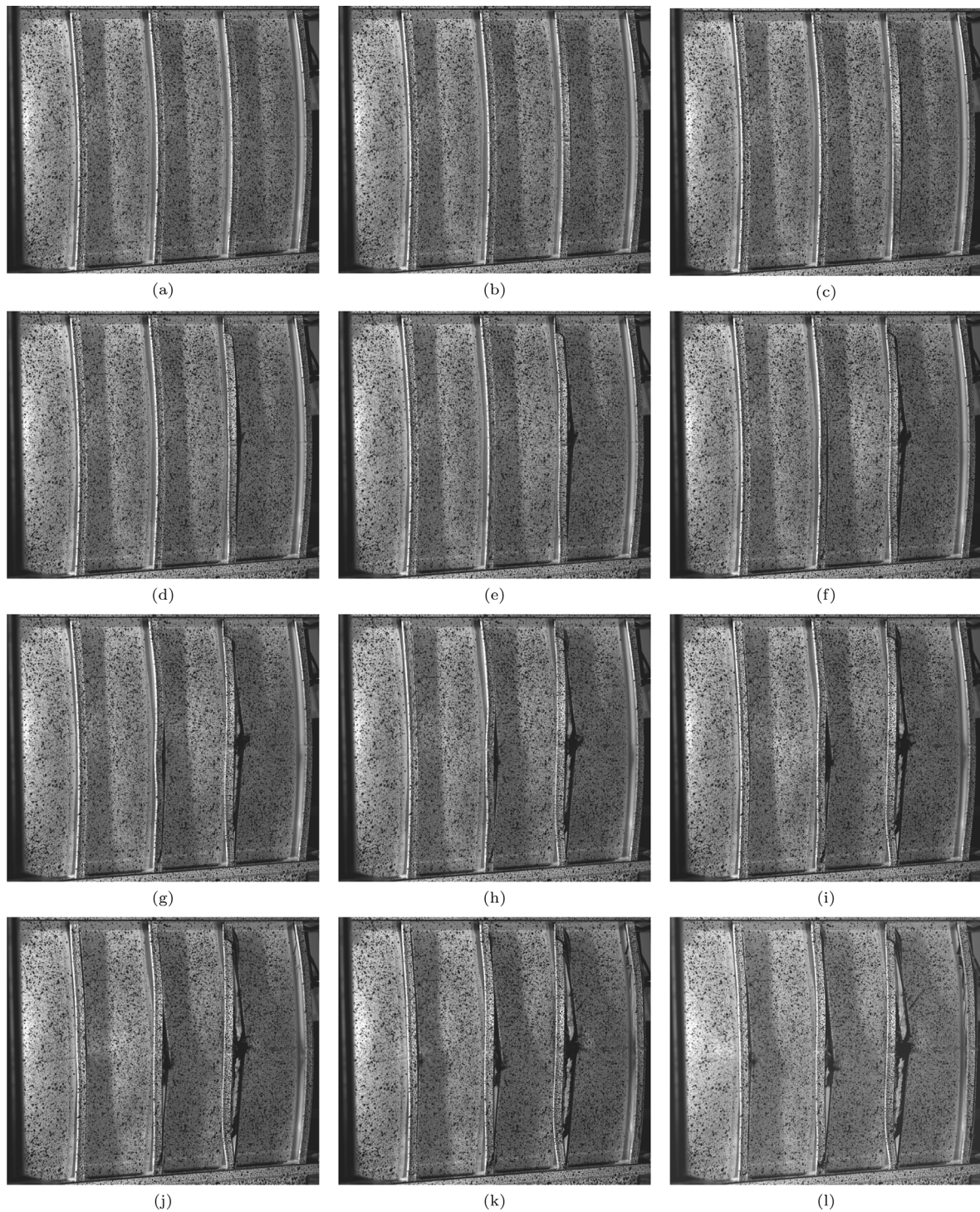
Fig. 13. High-speed footage panel 1: (a–b–c) stringer 4 cap separation; (d) stringer 4 web fracture; (e–f) stringer 4 cap separation; (g) stringer 3 web fracture; (h) stringer 2 cap separation; (i) stringer 5 butt-joint failure; (j–k) stringer 2 web fracture, stringer 5 cap separation; (l) stringer 5 web failure.

of stringer 3 fails next, and the web of stringer 2 shows delaminated plies at the web-cab interface (g). The cap of stringer 2 then separates almost completely from the web within one frame (h). The butt-joint of stringer 5 is the first visible skin–stringer interface that shows failure (i), with the failure occurring at the top of the panel. Due to the separation of the caps from the webs, most butt-joints can no longer be seen. After the butt-joint failure, the cap of stringer 5 separates from the web, simultaneously with the web fracture of stringer 2 (j–k). Lastly, the web of stringer 5 fails (l).

The frames of the high-speed footage are further analysed. When the caps separate from the web, the caps displace towards the skin in the middle of the panel. The caps hit the skin once or multiple times, with the skin also displacing out-of-plane in waves. When web fracture occurs, a few caps detach further and pull partially out of the potting material. After failure is completed, the caps return close to their initial position.

The panel collapse sequence of panel 2 is reported in Fig. 14 over a total time period of 2.3 ms, as every 2nd frame is reported. Panel collapse starts with the separation of the cap of stringer 2 in the middle
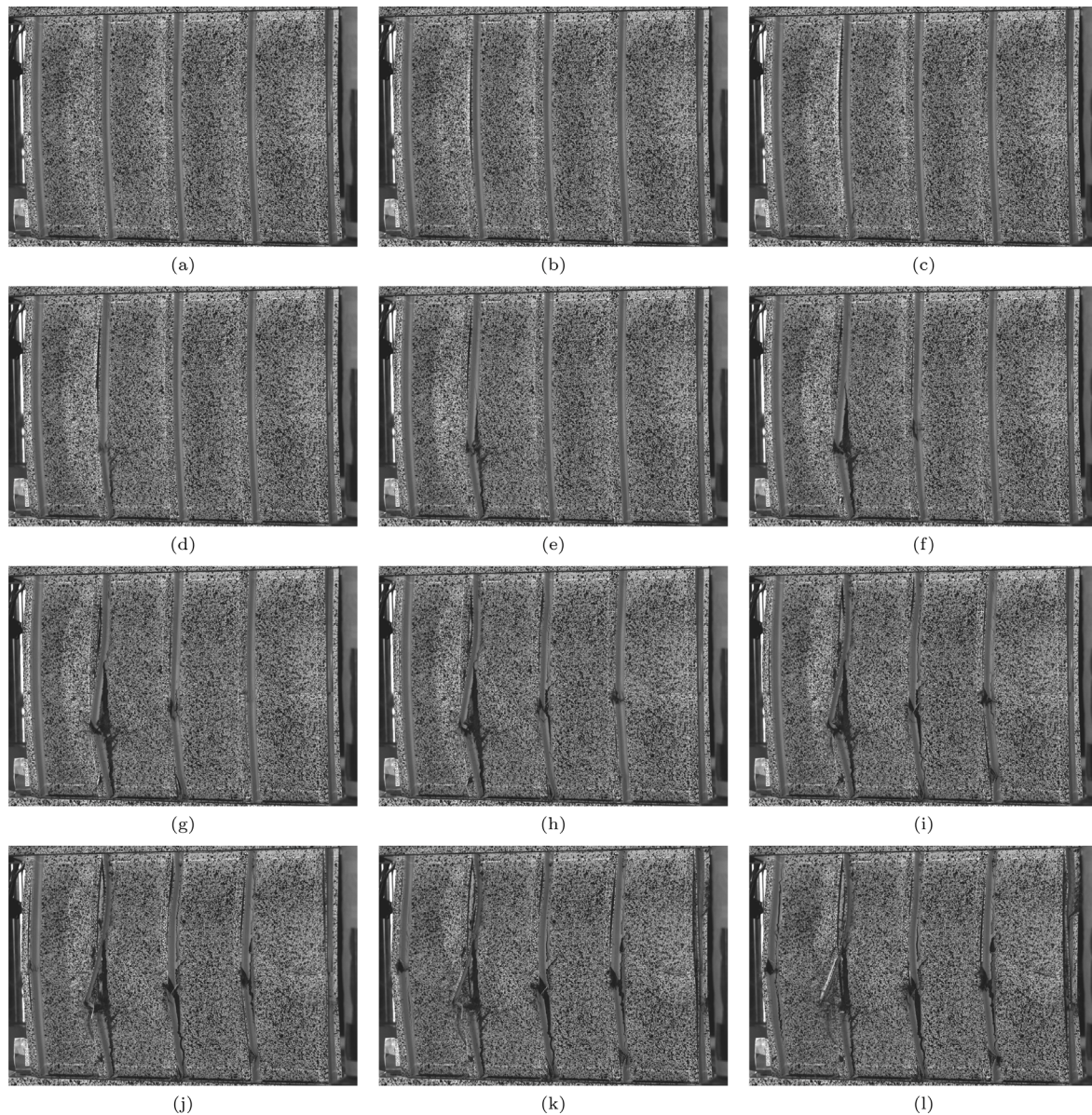
Fig. 14. High-speed footage panel 2: (a–b) stringer 2 cap separation; (c) stringer 2 butt-joint failure; (d) stringer 2 web fracture; (e) stringer 3 cap separation; (f) stringer 3 butt-joint and web failure, stringer 4 cap separation; (g) stringer 4 butt-joint failure; (h–i) stringer 4 fracture, stringer 1 cap separation; (j) stringer 5 cap separation, stringer 1 web fracture; (k) stringer 1 and 5 butt-joint failure; (l) stringer 5 web fracture.

of the panel (a–b), with a fracture in the cap at the bottom of the panel. The butt-joint of stringer 2 then separates from the skin at the bottom of the panel (c), which grows in an upward direction and is followed by fracture of the web (d). The cap of stringer 2 then separates from the web and fractures at the bottom of the panel (e). The butt-joint of stringer 2 fails at two locations, in the middle and bottom of the panel, and the web fractures (f). In the same frame, the cap of stringer 4 starts to separate, followed by further separation and fracture of the cap and failure in the butt-joint (g). The web of stringer 4 then separates, while the cap of stringer 1 also separates from the web (h–i). The web of stringer 1 then fails and the cap of stringer 5 separates from the web (j). The butt-joint of both stringer 1 and 5 then fails (k), and lastly, the web of stringer 5 fractures (l).

5.6. Post-failure investigation

Photos of panel 1 after failure are reported in Fig. 15(a–c). The caps, once separated from the webs, show fractures in several locations.

The caps of stringers 1, 2 and 5 are also partially pulled out from the potting material. The failure between cap and web seems to occur in two different ways, with the top ply of the web being delaminated and pulled off partially, and with separation between the web and the short fibre filler. In the middle of the panel, it seems that failure and delamination of the web plies is more common, with small pieces of the ply still attached to the cap, while towards the top and bottom of the panel, failure occurs at the interface between the web and short fibre filler. All the webs separated from the skin at the butt-joint. The webs present one or more fractures in each web and parts of the web are no longer attached to the panel. The failure in the web and skin region is mostly in the butt-joint. Stringer 1 has a part of the ply delaminated from the skin at the bottom of the panel, and the remaining butt-joints only show minimal pulled-off fibres. Failure in the butt-joint can be roughly divided into three types of failure: failure at the interface between skin and butt-joint, failure in the short fibre filler and failure at the interface between web and butt-joint. There are no visible fractures in the skin, but there is likely damage inside the laminate. There are indications of damage at the back of the skin, with paint chipped off.

Fig. 15. Post-failure photos: (a) panel 1 left-view; (b) panel 1 right-view; (c) panel 1 side-view; (d) panel 2 left-view; (e) panel 2 right-view; (f) panel 2 side-view.

Photos of panel 2 after failure are reported in Fig. 15(d–f). The failure modes, that are initially visible, are similar to panel 1. Stringer 2 fails first and has considerable amounts of fibre pullout from the skin, especially towards the top of the panel. The biggest difference, however, is that the edge of the skin, on the side of stringer 5, shows a large fracture. A close-up picture of this fracture is reported in Fig. 16. The skin is fractured across the thickness of the laminate and has a visible length of approximately 60 mm as seen from the stringer-side of the panel. Further propagation is visible on the back side of the skin, with propagation in a downward direction, leading to a total visible length of approximately 100 mm.

Both panels show failure first in the web-cap joint area. The cap-web failure of panel 1 occurs in the stringer with a BVID in the butt-joint, but the BVID itself is not necessarily critical, with no indication of crack growth before panel collapse. From panel 1, a close-up of the stringer 4 cap and of the web is reported in Fig. 17(a–b). There are web plies still attached to the cap (Fig. 17(a)), both the −45 ply (blue arrow) and parts of the 90 ply (red arrow), and the 45 ply (purple arrow) is visible on the web (Fig. 17(b)). This indicates that the critical failure mode is a combination of both the failure of these plies and delamination. Panel 2 fails in stringer 2, and the criticality of this stringer out of the three middle stringers is most likely due to imperfections. The stringer 2 web of panel 2, as reported in Fig. 17(c), shows similar damage as stringer 4 of panel 1. The 45 ply (purple arrow) is visible at the top of the web, as the −45 ply (blue arrow) and 90 ply (red arrow) present failure as well as delamination, indicating the same failure mode as panel 1.

Although the numerical model is not able to predict the sudden failure of the panel, as it does not take into account delamination between each ply, it is able to correctly identify the critical plies. Contour plots of the Hashin matrix tensile damage variable are reported in Fig. 18 for the middle three webs (a), the skin (b) and the full panel (c). The top −45 ply is most critical in the web, closely followed by the 45 ply. At 5.26 mm of displacement, the area with a damage variable

Fig. 16. Skin fracture of panel 2.

higher than 0.99 for the −45 ply reaches the bottom of the cap-web joint. This means that the short fibre filler joint is locally connected only to a failed ply, at the free edge of the web laminate.

The skin also has areas with a damage variable above 0.99, and the top 45 ply is the most critical. However, this can be considered less critical than the web, as the top skin plies are in tension, with no free edge and continuous fibres underneath the joint, making it less likely for this ply to delaminate compared to the web plies.

6. Concluding remarks

Two curved multi-stringer panels with butt-joint and roller boundary conditions were successfully tested and analysed, with one panel in pristine condition and one with initial damage in the butt-joint representing BVID.
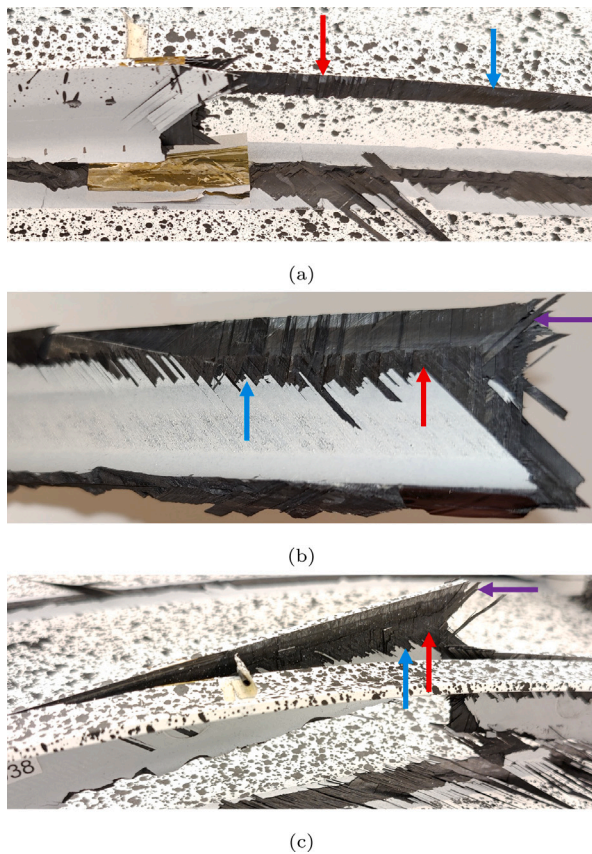
Fig. 17. Fracture photos: (a) panel 1 web and stringer; (b) panel 1 web; (c) panel 2 web and cap.

Fig. 18. Matrix tensile damage variable contour plot, at 5.26 mm of displacement: (a) middle three webs; (b) skin; (c) panel.

The load–displacement behaviour of the panels shows a gradual decrease in stiffness for an increase in applied displacement due to the initial curvature, roller boundary condition and buckling of the bays. The bays show a single half-wave buckling shape, with a slight variation in out-of-plane displacement between the bays, due to the anti-symmetric stringer and a small loading imperfection. The load–displacement curve starts to plateau at higher applied displacement, followed by panel collapse. The panels can sustain considerably high strains before failure, up to 19 400 microstrain. The panels fail when the caps separate from the web, followed by failure in the skin–stringer butt-joint and web fracture.

Three different approximations of the roller boundary conditions were analysed and compared, and the Hashin damage criterion is included in the analysis to determine damage initiation followed by evolution.

The analysis can predict the load–displacement and buckling behaviour well, but cannot predict the panel collapse and sudden loss of load-carrying capability due to the cap-web failure. The model with VCCT for skin–stringer separation predicts a conservative failure load, which might be caused by the idealized BVID with frictionless contact. Predicting the cap-web failure would require a more detailed model to allow each ply to delaminate. However, the model predicts the correct critical plies and shows that these have almost fully softened in the joint area, close to the failure displacement of the tests. This shows great promise for the ability to predict such a complex test and failure behaviour.

This research demonstrates that the roller boundary conditions approximate a loading condition that is likely to be more representative of aeronautical flight, and showcase the excellent capabilities of thermoplastic composites for primary structures in post-buckling. The test design also allowed for capturin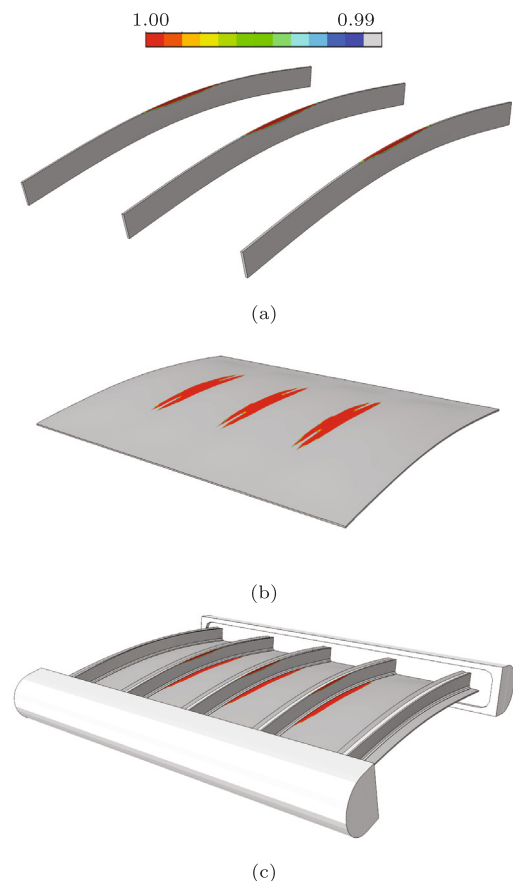g a critical failure mode that had not been previously investigated in literature. It is a valuable addition to the classical compression test, investigating the possibility of safely flying in post-buckling conditions in the future.

CRediT authorship contribution statement

Kevin van Dooren: Conceptualization, Methodology, Software, Validation, Investigation, Data Curation, Visualization, Writing – original draft. **Jan Waleson:** Conceptualization, Methodology, Resources. **Mark Chapman:** Conceptualization, Methodology, Resources. **Chiara Bisagni:** Conceptualization, Methodology, Investigation, Resources, Writing – Review & Editing, Supervision, Project administration.

Declaration of competing interest

The authors declare that they have no known competing financial interests or personal relationships that could have appeared to influence the work reported in this paper.

Data availability

Data will be made available on request.

References

[1] K. van Dooren, B. Tijs, J. Waleson, C. Bisagni, Skin-stringer separation in post-buckling of butt-joint stiffened thermoplastic composite panels, Compos. Struct. 304 (2023) 116294, http://dx.doi.org/10.1016/j.compstruct.2022.116294.

[2] K. van Dooren, C. Bisagni, Design, analysis and testing of thermoplastic welded stiffened panels to investigate skin-stringer separation in post-buckling, Composites B 267 (2023) 111033, http://dx.doi.org/10.1016/j.compositesb.2023.111033.

[3] J.R. Reeder, An evaluation of mixed-mode delamination failure criteria, 1992, NASA Technical Memorandum, NASA-TM-104210.

[4] W. Tan, B.G. Falzon, Modelling the crush behaviour of thermoplastic composites, Compos. Sci. Technol. 134 (2016) 57–71, http://dx.doi.org/10.1016/j.compscitech.2016.07.015.

[5] B.H.A.H. Tijs, M.H.J. Doldersum, A. Turon, J.E.A. Waleson, C. Bisagni, Experimental and numerical evaluation of conduction welded thermoplastic composite joints, Compos. Struct. 281 (2022) 114964, http://dx.doi.org/10.1016/j.compstruct.2021.114964.

[6] C.B. Brito, J. Teuwen, C. Dransfeld, I. F. Villegas, On improving process efficiency and weld quality in ultrasonic welding of misaligned thermoplastic composite adherends, Compos. Struct. 304 (2023) 116342, http://dx.doi.org/10.1016/j.compstruct.2022.116342.

[7] J.W. van Ingen, Thermoplastic orthogrid fuselage shell, SAMPE J. 52 (5) (2016) 7–15.

[8] S.L. Omairey, S. Sampethai, L. Hans, C. Worrall, S. Lewis, D. Negro, T. Sattar, E. Ferrera, E. Blanco, J. Wighton, et al., Development of innovative automated solutions for the assembly of multifunctional thermoplastic composite fuselage, Int. J. Adv. Manuf. Technol. 117 (5) (2021) 1721–1738, http://dx.doi.org/10.1007/s00170-021-07829-2.

[9] B.G. Falzon, K.A. Stevens, G.O. Davies, Postbuckling behaviour of a blade-stiffened composite panel loaded in uniaxial compression, Composites A 31 (2000) 459–468, http://dx.doi.org/10.1016/s1359-835x(99)00085-8.

[10] Y. Mo, D. Ge, J. Zhou, Experiment and analysis of hat-stringer-stiffened composite curved panels under axial compression, Compos. Struct. 123 (2015) 150–160, http://dx.doi.org/10.1016/j.compstruct.2014.11.074.

[11] L. Zhao, K. Wang, F. Ding, T. Qin, J. Xu, F. Liu, J. Zhang, A post-buckling compressive failure analysis framework for composite stiffened panels considering intra-, inter-laminar damage and stiffener debonding, Results Phys. 13 (2019) 102205, http://dx.doi.org/10.1016/j.rinp.2019.102205.

[12] L. Kootte, A Methodology to Reproduce Postbuckling in Composite Panels to Study Skin Stringer Separation, (Ph.D. thesis), Delft University of Technology, 2023, http://dx.doi.org/10.4233/uuid:cfccc1dc-df8a-4a49-8c1a-c2ebad7a1867.

[13] A. Raimondo, S.A. Doesburg, C. Bisagni, Numerical study of quasi-static and fatigue delamination growth in a post-buckled composite stiffened panel, Compos. Part B 182 (2020) (2020) 107589, http://dx.doi.org/10.1016/j.compositesb.2019.107589.

[14] C.G. Dávila, C. Bisagni, Fatigue life and damage tolerance of postbuckled composite stiffened structures with indentation damage, J. Compos. Mater. 52 (7) (2017) 931–943, http://dx.doi.org/10.1177/0021998317715785.

[15] R. Krueger, J.G. Ratcliffe, P.J. Minguet, Panel stiffener debonding analysis using a shell/3D modeling technique, Compos. Sci. Technol. 69 (14) (2009) 2352–2362, http://dx.doi.org/10.1016/j.compscitech.2008.12.015.

[16] C. Bisagni, R. Vescovini, C.G. Dávila, Single-stringer compression specimen for the assessment of damage tolerance of postbuckled structures, J. Aircr. 48 (2) (2011) 495–502, http://dx.doi.org/10.2514/1.C031106.

[17] J. Action, F.A. Leone, Progressive damage failure analysis of a multi-stringer post-buckled panel, in: AIAA SciTech 2020 Forum, (no. 2020–1481) 2020, http://dx.doi.org/10.2514/6.2020-1481.

[18] J. Paz, A. Raimondo, C. Bisagni, Experimental study of post-buckled single-stringer composite specimens under fatigue loads with different load levels and load ratios, Composites B (2023) 110606, http://dx.doi.org/10.1016/j.compositesb.2023.110606.

[19] W. Wagner, C. Balzani, Prediction of the postbuckling response of composite airframe panels including ply failure, Eng. Fract. Mech. 77 (18) (2010) 3648–3657, http://dx.doi.org/10.1016/j.engfracmech.2010.05.009.

[20] A.C. Orifici, I.O. de Zarate Alberdi, R.S. Thomson, J. Bayandor, Compression and post-buckling damage growth and collapse analysis of flat composite stiffened panels, Compos. Sci. Technol. 68 (2008) 3150–3160, http://dx.doi.org/10.1016/j.compscitech.2008.07.017.

[21] X. Wang, W. Cao, C. Deng, P. Wang, Z. Yue, Experimental and numerical analysis for the post-buckling behavior of stiffened composite panels with impact damage, Compos. Struct. 133 (2015) 840–846, http://dx.doi.org/10.1016/j.compstruct.2015.08.019.

[22] J. Zou, Z. Lei, R. Bai, D. Liu, H. Jiang, J. Liu, C. Yan, Damage and failure analysis of composite stiffened panels under low-velocity impact and compression after impact, Compos. Struct. 262 (2021) 113333, http://dx.doi.org/10.1016/j.compstruct.2020.113333.

[23] S. Lauterbach, A. Orifici, W. Wagner, C. Balzani, H. Abramovich, R. Thomson, Damage sensitivity of axially loaded stringer-stiffened curved CFRP panels, Compos. Sci. Technol. 70 (2) (2010) 240–248, http://dx.doi.org/10.1016/j.compscitech.2009.10.013.

[24] J.W. van Ingen, J.E.A. Waleson, A. Offringa, M. Chapman, Double curved thermoplastic orthogrid rear fuselage shell, in: SAMPE Europe Conference. Nantes, France, 2019, pp. 1–10.

[25] W.D. Kroll, L. Mordfin, W.A. Garland, Investigation of sandwich construction under lateral and axial loads, 1953, NACA Technical Note, NACA-TN-3090.

[26] C. Chang, M. Timmons Jr., Compression tests of sandwich panels with facings at different temperatures: Experimental deflection pattern found to correlate well with the assumed orthogonal sine-wave deflection pattern, Exp. Mech. 2 (8) (1962) 249–256, http://dx.doi.org/10.1007/BF02326724.

[27] C. Meeks, E. Greenhalgh, B.G. Falzon, Stiffener debonding mechanisms in post-buckled CFRP aerospace panels, Composites A 36 (2005) 934–946, http://dx.doi.org/10.1016/j.compositesa.2004.12.003.

[28] C. Bisagni, C.G. Dávila, Experimental investigation of the postbuckling response and collapse of a single-stringer specimen, Compos. Struct. 19 (2014) 493–503, http://dx.doi.org/10.1016/j.compstruct.2013.09.018.

[29] G. Grondin, Q. Chen, A. Elwi, J. Cheng, Stiffened steel plates under compression and bending, J. Constr. Steel Res. 45 (2) (1998) 125–148, http://dx.doi.org/10.1016/S0143-974X(97)00058-9.

[30] Y. Tanaka, H. Endo, Ultimate strength of stiffened plates with their stiffeners locally buckled in compression, J. Soc. Naval Archit. Jpn. 1988 (164) (1988) 456–467.

[31] B.H. Choi, M. Hwang, T. Yoon, C.H. Yoo, Experimental study of inelastic buckling strength and stiffness requirements for longitudinally stiffened panels, Eng. Struct. 31 (5) (2009) 1141–1153, http://dx.doi.org/10.1016/j.engstruct.2009.01.010.

[32] A. Aalberg, M. Langseth, P. Larsen, Stiffened aluminium panels subjected to axial compression, Thin-Walled Struct. 39 (10) (2001) 861–885.

[33] Y. Zha, T. Moan, Experimental and numerical prediction of collapse of flatbar stiffeners in aluminum panels, J. Struct. Eng. 129 (2) (2003) 160–168, http://dx.doi.org/10.1061/(ASCE)0733-9445(2003)129:2(160).

[34] E. Hahn, L. Carlsson, B. Westerlind, Edge-compression fixture for buckling studies of corrugated board panels, Exp. Mech. 32 (1992) 252–258, http://dx.doi.org/10.1007/BF02319363.

[35] J.W. van Ingen, P. Lantermans, I. Lippers, Impact behaviour of a butt jointed thermoplastic stiffened skin panel, in: SAMPE 2012 International Symposium and Exhibition, 2012.

[36] Abaqus 2021 documentation, Dassault Systemes Simulia Corp, 2021.

[37] Z. Hashin, A. Rotem, A fatigue failure criterion for fiber reinforced materials, J. Compos. Mater. 7 (4) (1973) 448–464, http://dx.doi.org/10.1177/002199837300700404.

[38] I. Lapczyk, J.A. Hurtado, Progressive damage modeling in fiber-reinforced materials, Composites A 38 (11) (2007) 2333–2341, http://dx.doi.org/10.1016/j.compositesa.2007.01.017.

[39] I. Baran, L.L. Warnet, R. Akkerman, Assessment of failure and cohesive zone length in co-consolidated hybrid C/PEKK butt joint, Eng. Struct. 168 (2018) 420–430, http://dx.doi.org/10.1016/j.engstruct.2018.04.089.

[40] J. Bertolini, B. Castanié, J.J. Barrau, J.P. Navarro, Multi-level experimental and numerical analysis of composite stiffener debonding. Part 1: Non-specific specimen level, Compos. Struct. 90 (4) (2009) 381–391, http://dx.doi.org/10.1016/j.compstruct.2009.04.001.

[41] R. Krueger, An approach to assess delamination propagation simulation capabilities in commercial finite element codes, 2008, NASA Technical Memorandum, NASA/TM-2008-215123.

[42] M.L. Benzeggagh, M. Kenane, Measurement of mixed-mode delamination fracture toughness of unidirectional glass/epoxy composites with mixed-mode bending apparatus, Compos. Sci. Technol. 56 (1996) 439–449, http://dx.doi.org/10.1016/0266-3538(96)00005-x.

[43] P.P. Camanho, C.G. Dávila, M.F. de Moura, Numerical simulation of mixed-mode progressive delamination in composite materials, J. Compos. Mater. 37 (16) (2003) 1415–1438, http://dx.doi.org/10.1177/0021998303034505.